Corrected 20 November 2015; see full text.

SOLAR CELLS

Efficient and stable large-area perovskite solar cells with inorganic charge extraction layers

Wei Chen,[1,2]* Yongzhen Wu,[1]* Youfeng Yue,[1] Jian Liu,[1] Wenjun Zhang,[2] Xudong Yang,[3] Han Chen,[3] Enbing Bi,[3] Islam Ashraful,[1] Michael Grätzel,[4]† Liyuan Han[1,3]†

The recent dramatic rise in power conversion efficiencies (PCEs) of perovskite solar cells (PSCs) has triggered intense research worldwide. However, high PCE values have often been reached with poor stability at an illuminated area of typically less than 0.1 square centimeter. We used heavily doped inorganic charge extraction layers in planar PSCs to achieve very rapid carrier extraction, even with 10- to 20-nanometer-thick layers, avoiding pinholes and eliminating local structural defects over large areas. The robust inorganic nature of the layers allowed for the fabrication of PSCs with an aperture area >1 square centimeter that have a PCE >15%, as certified by an accredited photovoltaic calibration laboratory. Hysteresis in the current-voltage characteristics was eliminated; the PSCs were stable, with >90% of the initial PCE remaining after 1000 hours of light soaking.

Organic-inorganic metal halide perovskite solar cells (PSCs) have attracted attention as a result of the meteoric rise in their solar-to-electric power conversion efficiencies (PCEs) over the past few years (*1*). In particular, methylammonium ($CH_3NH_3PbI_3$, denoted as $MAPbI_3$) and formamidinium lead iodide [$CH(NH_2)_2PbI_3$] emerged as highly attractive solar light–harvesting materials because of their intense broadband absorption, high charge carrier mobility, low-cost precursor materials, and simple solution processing (*2*, *3*). Their ambipolar semiconducting characteristics further enable variable device architectures, ranging from mesoscopic to planar structures with n-i-p or p-i-n layouts (*4*). Mesoporous TiO_2-based PSCs have reached the highest performance levels thus far (*5*–*7*), with a certified PCE of 20.1% (*8*). However, there is growing interest in inverted (p-i-n) planar device architectures that typically use a $MAPbI_3$-PCBM ([6,6]-phenyl-C_{61}-butyric acid methyl ester) bilayer junction, because of their simple fabrication and relatively small hysteresis (*9*–*11*). The true PCE and stability of planar PSCs remain open to debate, because these devices have not previously been certified and their stability has been largely unexplored. Only hole-conductor–free mesoscopic PSCs using carbon as a back contact have hitherto shown promising stability under long-term light soaking and long-term heat exposure, but their certified PCE remains relatively low at 12.8% (*12*, *13*).

Regardless of their architectures, all high-efficiency PSCs thus far have had small areas, with device sizes often <0.1 cm^2 (table S1) (*14*). Because such a small device size is likely to cause measurement errors, an obligatory minimum cell area of >1 cm^2 is required for certified PCEs to be recorded in the standard solar cell efficiency tables edited by public test centers, such as the National Renewable Energy Laboratory in the United States and the National Institute of Advanced Industrial Science and Technology (AIST) in Japan (*15*). It has been recommended that the efficiencies should be recorded with cell sizes of ideally 1 to 2 cm^2 or larger to allow comparison with competing technologies (*16*–*19*). Although a few studies have reported attempts to fabricate centimeter-scale PSCs—for example, by using a vacuum evaporation system (*20*) or modified two-step approach (*21*) to produce large-area $MAPbI_3$ films—the PCEs obtained for these devices reached only 10.9 to 12.6%. Apart from the small device areas, the widely recognized hysteresis and stability issues of PSCs have raised doubts about the reliability of previously claimed high efficiencies (*22*, *23*).

The poor reproducibility and lack of uniformity of PSCs make it challenging to obtain high efficiencies with large devices. It is difficult to control the formation of cracks and pinholes in the selective carrier extraction layers over large areas. Because small-size PSCs typically show a wide spread in their PCEs, previous work has focused on improving the uniformity of the perovskite layer by varying its deposition methods (*3*, *6*, *10*). However, fewer studies have aimed at identifying selective extraction layers for photogenerated charge carriers placed over the current collector to prevent their recombination at its surface (*24*–*26*), even though such selective contacts have turned out to be equally important to developing efficient solar-light harvesters (*27*). The dilemma with optimizing such charge carrier extraction layers in solar cells is that the film should be thin to minimize resistive losses, while at the same time, it should cover the entire collector area in a contiguous and uniform manner. Meeting these requirements becomes increasingly difficult as the device area increases.

Here we present a strategy that addresses simultaneously the scale-up and stability issues facing current PSC embodiments. We developed heavily p-doped (p^+) $Ni_xMg_{1-x}O$ and n-doped (n^+) TiO_x contacts to extract selectively photogenerated charge carriers from an inverted planar $MAPbI_3$-PCBM film architecture. We implemented the p- and n-doping by substituting $Ni(Mg)^{2+}$ ions and Ti^{4+} ions on the $Ni_xMg_{1-x}O$ lattice and TiO_x matrix with Li^+ and Nb^{5+} ions, respectively. The resulting dramatic increase in the electrical conductivity enabled 10- to 20-nm-thick oxide layers to be used for selective extraction of one type of charge carrier, while improving the electronic blocking effect for the other type by reducing the density of pinholes and cracks over large areas. Accordingly, the series resistance (R_s) of the oxides decreased and the shunt resistance (R_{sh}) greatly increased with respect to the undoped layers, leading to an excellent fill factor (FF), with values exceeding 0.8, and hysteresis-free behavior. With this strategy, we successfully fabricated large-size (>1 cm^2) PSCs with an efficiency of up to 16.2%. A PCE of 15% was certified by a public test center (Calibration, Standards and Measurement Team at the Research Center for Photovoltaics, AIST). This is listed as the first official efficiency entry for PSCs in the most recent edition of the solar cell efficiency tables (*28*). Moreover, the devices based on these stable p^+ and n^+ inorganic metal-oxide charge extraction layers show high stability, rendering them attractive for future practical deployment of PSCs.

We fabricated PSCs with an inverted planar device architecture (Fig. 1A); a cross-sectional scanning electron microscopy (SEM) image of this architecture is shown in Fig. 1B. We first deposited the NiO-based hole extraction layer onto fluorine-doped tin oxide (FTO) glass by means of spray pyrolysis. The precursor solution was composed of nickel (II) acetylacetonate, either alone or together with doping cations (Mg^{2+} from magnesium acetate tetrahydrate and Li^+ from lithium acetate) in a super-dehydrated acetonitrile and ethanol mixture. The $MAPbI_3$ perovskite layer, with a thickness of ~300 nm, was deposited using a reported method (*6*); this was followed by the deposition of a thin PCBM layer (80 nm), accomplished by spin-coating its chlorobenzol solution (20 mg ml^{-1}) at 1000 rpm for 30 s. An n-type TiO_x-based electron

---

[1] Photovoltaic Materials Unit, National Institute for Materials Science, Tsukuba, Ibaraki 305-0047, Japan. [2] Michael Grätzel Centre for Mesoscopic Solar Cells, Wuhan National Laboratory for Optoelectronics, Huazhong University of Science and Technology, Wuhan, China. [3] State Key Laboratory of Metal Matrix Composites, Shanghai Jiao Tong University, 800 Dong Chuan Road, Minhang District, Shanghai 200240, China. [4] Laboratory of Photonics and Interfaces, Department of Chemistry and Chemical Engineering, Swiss Federal Institute of Technology, Station 6, CH-1015 Lausanne, Switzerland.
***These authors contributed equally to this work.**
†Corresponding author. E-mail: michael.graetzel@epfl.ch (M.G.); han.liyuan@nims.go.jp (L.H.)

Corrected 20 November 2015; see full text.

extraction layer with and without Nb^{5+} doping was further deposited on the PCBM by spin-coating a diluted methanol solution of titanium isopropoxide (alone or mixed with niobium ethoxide), followed by controlled hydrolysis and condensation (*14*). Finally, the device was completed by thermal evaporation of a 100-nm-thick Ag cathode. The band alignments of relevant functional layers are shown in Fig. 1C, based on the energy levels determined by ultraviolet (UV) photoelectron spectroscopy and UV-visible absorption spectroscopy measurements (fig. S1) (*14*). The uniformity of the perovskite and PCBM layers was examined by means of cross-sectional SEM (fig. S2) (*14*). The full x-ray photoelectron spectroscopy (XPS) spectra of the NiO- and TiO_x-based charge carrier extraction layers are shown in fig. S3 (*14*), revealing the designated compositions for the target materials. A close-up view of the morphology of the charge carrier extraction layers is shown in fig. S4 (*14*). Their pinhole densities were examined by electrical measurement, as discussed below.

The stoichiometric form of NiO is a wide-band-gap semiconductor with a very low intrinsic conductivity of 10^{-13} S cm^{-1} (*29*). Self-doping by introducing Ni^{3+} acceptors into the NiO crystal lattice renders the crystals more conductive, depending on the film deposition techniques and conditions (*11*, *30*–*32*). The room-temperature specific conductivity of our NiO films, derived from Hall effect measurements, was 1.66×10^{-4} S cm^{-1}. This value is much lower than that of the typically used p-type contact layer of PEDOT:PSS [poly(3,4-ethylenedioxythiophene) polystyrene sulfonate], which has a conductivity of 1 to 1000 S cm^{-1} (*33*). The low conductivity of NiO leads to a high R_s, resulting in a low FF for the solar cells (*34*). Substitutional doping with Li^+ is an effective way to increase the p-conductivity of NiO (*35*). Values of heavily p-doped NiO films can reach 1 to 10 S cm^{-1} at room temperature under optimal conditions (*36*). For our Li^+-doped $Ni_xMg_{1-x}O$ films, the conductivity is 2.32×10^{-3} S cm^{-1}, ~12 times greater than that of the undoped reference.

A Mg^{2+} content of 15 mole percent (mol %) was alloyed in the Li^+-doped nickel oxide film, to compensate for the undesirable positive shift of its valence band energy (E_{VB}) caused by incorporation of Li^+ into the lattice (fig. S1) (*14*, *35*, *37*, *38*). The Li^+ content was adjusted to 5 mol %, giving the doped oxide the formula of $Li_{0.05}Mg_{0.15}Ni_{0.8}O$, assuming that the molar ratio of the three different cations in the spray pyrolysis solution was maintained in the mixed oxide. This codoping strategy is feasible because the mismatch of the ionic radii of Li^+ (0.76 Å), Mg^{2+} (0.71 Å), and Ni^{2+} (0.69 Å) is small, conferring good lattice stability to the $Li_xMg_yNi_{1-x-y}O$ ternary oxides. We compared the conductivity of the NiO and $Li_{0.05}Mg_{0.15}Ni_{0.8}O$ films using the contact-current mode of a scanning probe microscope (SPM) (Fig. 2, A and B). At a bias potential of 1.0 V, the electric current increased by a factor of ~10 (from ~0.3 nA to ~3 nA) upon replacing undoped NiO with a $Li_{0.05}Mg_{0.15}Ni_{0.8}O$ film. The XPS spectra in fig. S6 (*14*) reveal that the doping increased the relative content of Ni^{3+} acceptors in the $Li_{0.05}Mg_{0.15}Ni_{0.8}O$ sample. These findings are consistent with findings for Li^+-doped NiO films reported in (*32*), and they explain the increase in carrier concentration from 2.66×10^{17} cm^{-3} in the undoped NiO film to 6.46×10^{18} cm^{-3} in the $Li_{0.05}Mg_{0.15}Ni_{0.8}O$ film, which we derived from Hall effect measurements.

The electron specific n-type TiO_x contact commonly used for organic photovoltaic devices is normally fabricated by hydrolysis and condensation of titanium alkoxides at temperatures below 150°C (*39*, *40*), where the crystallization of TiO_2 is slow. In order to prevent heat-induced degradation of the perovskite layer and the adjacent interfaces, we kept the annealing temperature of TiO_x films below 70°C. Although such TiO_x films have been used extensively in organic photovoltaic devices, the details of their structure and mechanism of electric conduction so far have not been elucidated (*41*). One commonly recognized problem is that the amorphous nature of TiO_x leads to extremely low specific conductivities that are in the range of 10^{-8} to 10^{-6} S cm^{-1} (*42*). Nb^{5+} doping has proved to be effective for enhancing the conductivity of crystalline anatase TiO_2 films to ~10^4 S cm^{-1}, enabling its use as a transparent conducting oxide similar to conventional indium tin oxide (ITO) (*43*). By analogy, this dopant is expected to also improve the conductivity of the amorphous TiO_x via substitution of Ti^{4+} with Nb^{5+}, which is expected to create donor centers. From the current-voltage (*I-V*) curves obtained from SPM measurements (Fig. 2B), the conductivity of the TiO_x film was estimated to increase from about 10^{-6} S cm^{-1} to 10^{-5} S cm^{-1} upon adding 5 mol % Nb^{5+} to the precursor solution. By resolving the XPS spectra in fig. S6 (*14*), we

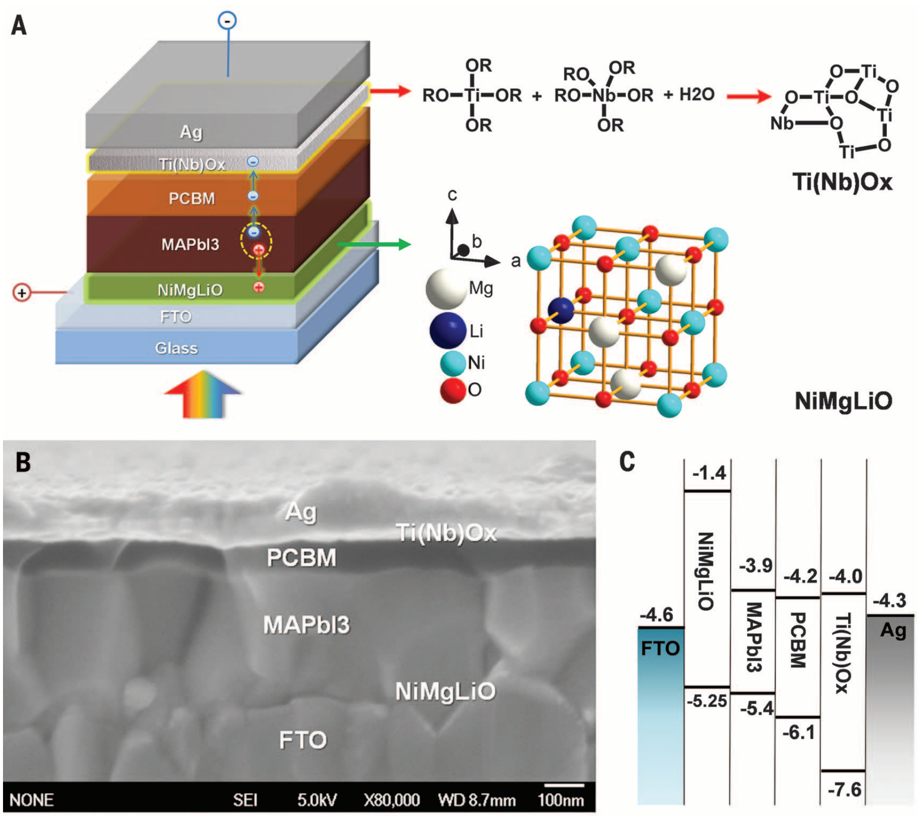

Fig. 1. Structure and band alignments of the PSC. (**A**) Diagram of the cell configuration highlighting the doped charge carrier extraction layers. The right panels show the composition of $Ti(Nb)O_x$ and the crystal structure of Li^+-doped $Ni_xMg_{1-x}O$, denoted as NiMg(Li)O. (**B**) A high-resolution cross-sectional SEM image of a complete solar cell [the corresponding energy-dispersive x-ray analysis results are shown in fig. S5 (*14*), demonstrating the presence of the p^+ $Ni_xMg_{1-x}O$ and n^+ TiO_x charge extraction layers]. (**C**) Band alignments of the solar cell. The data for $MAPbI_3$ and PCBM are taken from (*11*).

Corrected 20 November 2015; see full text.

observed that the relative content of Ti^{3+} in comparison with Ti^{4+} (i.e., the donor species in the TiO$_x$ film, responsible for its n-type conductivity) increased as a result of Nb^{5+} doping.

We derived the optimal thickness of the NiO- and TiO$_x$-based charge extraction layers from the electrical measurements shown in fig. S7 (*14*). A complete NiO or TiO$_x$ layer with no pinholes requires a thickness of at least 20 or 10 nm, respectively, regardless of the presence of dopants. These minimum thicknesses should depend on the surface chemistry and morphology of the underlayers (FTO for NiO or PCBM for TiO$_x$), as well as the fabrication methods used for the NiO and TiO$_x$ films. We compared small solar cells with sizes of 0.09 cm^2 and varied the NiO layer thickness from 10 to 20 to 40 nm, keeping that of the Ti$_{0.95}$Nb$_{0.05}$O$_x$ fixed at 10 nm. We fixed the Li$_{0.05}$Mg$_{0.15}$Ni$_{0.8}$O layer thickness at 20 nm and varied that of the TiO$_x$ films from 5 to 30 nm. For each condition, 20 cells were made and measured to establish any underlying trends. As shown in fig. S8 (*14*), although high performances occasionally can be achieved from devices with very thin charge carrier extraction layers (~10 nm for NiO or ~5 nm for TiO$_x$), most such devices had lower PCEs because of lower FFs and open-circuit voltages (V_{oc}) (fig. S9) (*14*), which can be attributed to the presence of substantial numbers of pinholes. The reproducibility of the device performance was greatly enhanced as the thickness of charge extraction layers increased, and the optimal performance was attained with 20-nm NiO and 10-nm TiO$_x$ films, in agreement with the electrical measurement. Further increasing the film thickness of the two charge extraction layers can lead to a large decline in efficiency caused by increased internal resistance, larger optical loss, or both (fig. S10) (*14*). Thus, we fixed the thickness of NiO and TiO$_x$ at 20 and 10 nm, respectively, for the studies described below of doping effect on device performance.

Figure 3A shows the effect of doping the NiO and TiO$_x$ charge extraction layers on the photocurrent density–voltage (*J-V*) curves of PSCs, measured under simulated air mass (AM)–1.5 sunlight with a forward scanning direction. The short-circuit current (J_{sc}), V_{oc}, FF, and PCE data are listed in table S2 (*14*). Doping of NiO and TiO$_x$ both reduced R_s and improved the FF and, to a lesser extent, J_{sc} and V_{oc}. The TiO$_x$ electron extraction layers mainly affected the shape of *J-V* curves in the forward bias range from 0.7 to 1.0 V, where a Schottky barrier–type contact between PCBM and Ag strongly restricted efficient electron collection (fig. S9A) (*14*, *44*). The Nb^{5+} doping of TiO$_x$ reduced the interfacial electron transfer resistance and facilitated electron transport, increasing the photocurrent, especially in the 0.7- to 1.0-V forward bias region. The NiMg(Li)O-based hole extraction layer promoted ohmic contact formation at the FTO-MAPbI$_3$ interface by decreasing the barrier height through the staircase energy level alignment shown in Fig. 1C. Heavy p-doping of NiO increased the electrical conductivity, decreasing the charge transport resistance and hence enhancing hole extraction.

Doping of both NiO and TiO$_x$ improved the cell performance by increasing the values of FF and V_{oc} to 0.827 and 1.083 V, respectively, leading to a PCE of 18.3% for this planar PSC with MAPbI$_3$. In comparison with PEDOT:PSS–based PSCs, the V_{oc} was higher by ~100 mV, indicating that with Li$_{0.05}$Mg$_{0.15}$Ni$_{0.8}$O, the holes can be extracted at a higher energy level (*10*). Furthermore, the FF of 0.827 is one of the highest values reported for PSCs (*8*, *9*, *23*), demonstrating the key role of the charge extraction layers in minimizing resistive losses and improving the photovoltaic performance.

To gain further insight into the reasons for the performance enhancement caused by the doping, we characterized the charge carrier extraction, transportation, and recombination by nanosecond time-resolved photoluminescence (PL) decay, using a picosecond laser flash as the excitation source, and by measuring transient photocurrent and photovoltage decays on the microsecond scale. The charge extraction in our cells includes the electron transfer from the MAPbI$_3$ absorber layer to the PCBM and TiO$_x$ layers, the hole transfer to NiO, and the carrier transport in the TiO$_x$ and NiO layers. The MAPbI$_3$/PCBM interface has been demonstrated to be very efficient for electron extraction (*9*–*11*). Doping of the TiO$_x$ extraction layer is unlikely to have a direct impact on the electron injection rate, because of its physical separation from the MAPbI$_3$ by the 80-nm-thick PCBM layer. Nevertheless, it greatly accelerates the electron extraction by decreasing the electron transport time, as shown in Fig. 3C. Figure 3B shows the PL decays of the MAPbI$_3$ films on different substrates, including a glass slide and NiO and Li$_{0.05}$Mg$_{0.15}$Ni$_{0.8}$O deposited on FTO glass. The MAPbI$_3$ itself showed a long PL lifetime of >100 ns, indicating slow carrier recombination in the perovskite layer (*10*). When brought into contact with the p-type hole extraction layers, the PL

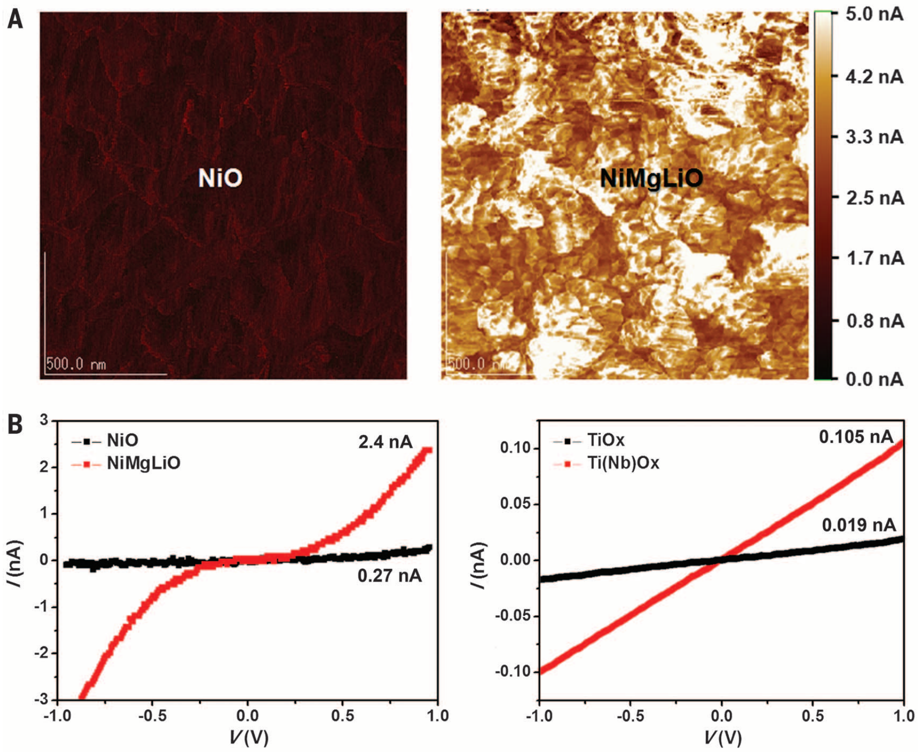

Fig. 2. Dopant-enhanced conductivity of NiO and TiO$_x$. (**A**) Comparison of the conductivity mapping results for NiO (left) and Li$_{0.05}$Mg$_{0.15}$Ni$_{0.8}$O (right) films. (**B**) Comparison of the *I-V* curves of NiO and Li$_{0.05}$Mg$_{0.15}$Ni$_{0.8}$O films deposited on FTO glass (left), and comparison of the *I-V* curves for TiO$_x$ and Ti$_{0.95}$Nb$_{0.05}$O$_x$ films deposited on PCBM-ITO glass (right), obtained by SPM measurements. The thickness was 20 nm for both NiO- and TiO$_x$-based films.

Corrected 20 November 2015; see full text.

lifetimes were shortened to a similar degree for both doped and undoped NiO-MAPbI$_3$ contacts. Thus, doping has a negligible influence on the hole injection.

We derived the charge transport and recombination time constants (τ_t and τ_r) from the transient photocurrent and photovoltage decays measured at the short and open circuit, respectively (Fig. 3C). The τ_t decreased fivefold from 4.41 μs for the undoped cell to 0.88 μs for the doped cell, confirming the much faster charge transport through the doped charge carrier extraction layers, compared to the undoped ones. However, we found that the τ_r of the doped cell was substantially longer than that of the undoped one (84.8 versus 50.5 μs; Fig. 3D), which we attribute to slower interfacial charge recombination, because the very rapid carrier extraction prevents charge accumulation at the interface of the pervovskite with the charge extraction layer. The doping-induced difference in charge transport and recombination kinetics should be the main factor responsible for the performance enhancement.

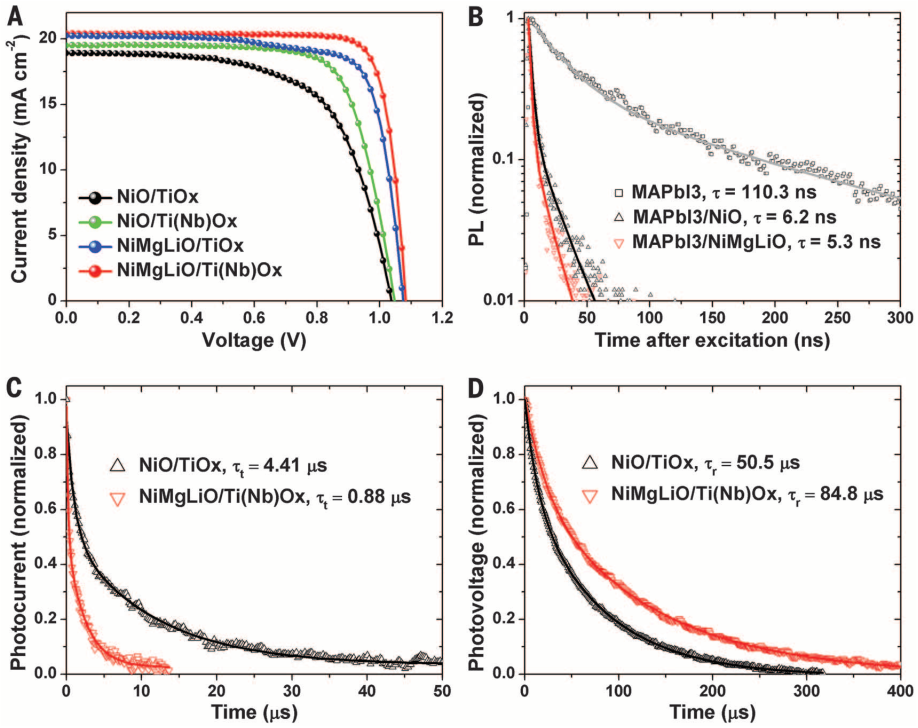

Fig. 3. Doping-enhanced photovoltaic performance. (**A**) *J-V* curves of solar cells based on different combinations of charge extraction layers with standard thicknesses [NiO, NiMg(Li)O, 20 nm; TiO$_x$ and Ti(Nb)O$_x$, 10 nm]. (**B**) Normalized PL transient decay curves of the MAPbI$_3$ layer on its own and MAPbI$_3$ at the controlled interfaces with NiO and NiMg(Li)O. Solid lines are fitted results with a double exponential decay. The time interval during which the PL decays to 1/*e* of the initial intensity is defined as the characteristic lifetime (τ) of free carriers after photoexcitation. (**C**) and (**D**) show normalized transient photocurrent and photovoltage decay curves, respectively, based on undoped and doped charge carrier extraction layers. The charge transport (τ_t) and recombination time (τ_r) are again defined as the time interval during which the photocurrent or photovoltage decays to 1/*e* of the its initial value immediately after excitation.

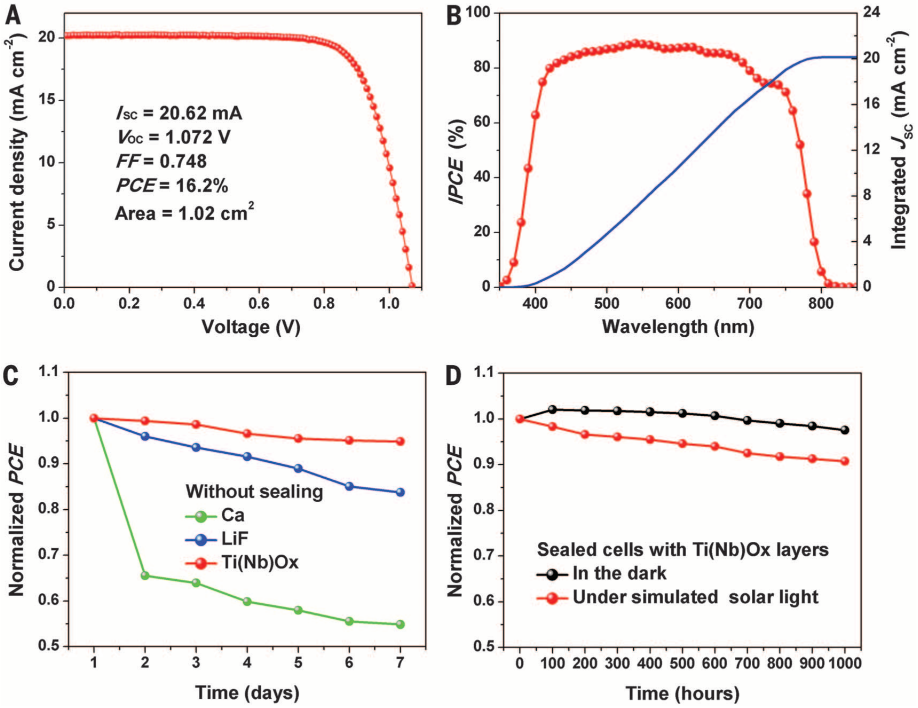

Fig. 4. Performance and stability of large-size cells. (**A**) *J-V* curve of the best large cell endowed with antireflection film. (**B**) The corresponding IPCE spectrum (red) and integrated J_{sc} (blue). (**C**) The stability of the cells without sealing, based on different electron extraction layers of Ca (4 nm), LiF (1.5 nm), and Ti(Nb)O$_x$ (10 nm) between PCBM and the Ag contact. The cells were kept in a dry cabinet (<20% humidity) in the dark and measured in ambient air. (**D**) Stability of sealed cells kept in the dark or under simulated solar light (AM 1.5; 100 mW cm^{-2}; using a 420-nm UV light cut-off filter; surface temperature of the cell, 45° to 50°C; bias potential, 0 V).

Corrected 20 November 2015; see full text.

We examined the hysteresis of our cells using different scan rates and directions. By decreasing the step width from 70 to 5 mV, the PCEs determined from the forward scan increased slightly from 18.14 to 18.35%. However, the reverse-scan PCEs decreased substantially from 22.35% at 70 mV/step (fig. S11A and table S3) (*14*) to 18.40% at 5 mV/step. The steady power outputs measurements (fig. S11D) (*14*) indicate that the PCEs obtained in forward scans and at small step widths (5 to 10 mV) are close to the real performance. The V_{oc} and PCE values obtained in a fast reverse scan (1.273 V and 22.35% at 70 mV/step) are largely overestimated. With the step widths of 5 to 10 mV, the PCE differences between forward and reverse scans are very small, within 0.3% in absolute PCE values, reflecting negligible hysteresis. A histogram comparing the difference in the PCEs obtained from scanning in the forward and reverse bias directions is shown in fig. S11C (*14*), supporting the absence of hysteresis for the optimized device architecture. In contrast, for undoped charge extraction layers, a pronounced hysteresis was observed even for slow scan rates (fig. S11E) (*14*), likely resulting from unbalanced charge accumulation at the two interfaces (*45*). Thus, the $Li_{0.05}Mg_{0.15}Ni_{0.8}O$ and $Ti_{0.95}Nb_{0.05}O_x$ charge extraction layers create robust low-impedance interfaces that can mitigate the *J-V* hysteresis under a routine scanning condition.

We fabricated cells with active areas >1 cm^2 as a first step toward the scale-up of the photovoltaic devices. Figure 4A shows the *J-V* curve of such a cell, with an aperture area of 1.02 cm^2. The cell has excellent performance, with J_{sc}, V_{oc}, and FF reaching values of 20.21 mA cm^{-2}, 1.072 V, and 0.748, respectively, corresponding to a PCE of 16.2%. Hysteresis for these large-area devices is also small (fig. S12) (*14*). The corresponding incident photon-to-current conversion efficiency (IPCE) (Fig. 4B) has a broad plateau with a maximum value of 90.1% over essentially the entire visible range. The integrated J_{sc} calculated from the IPCE matches well with the measured value. Compared with small-size cells (0.09 cm^2), a ~10% decrease in PCE was observed in large-size cells (1.02 cm^2), which is mainly caused by the large sheet resistance of the FTO. We sent one of our best large cells to a public test center (AIST) for certification. A PCE of 15.0% for a 1.017-cm^2 device was certified (fig. S13) (*14*).

To demonstrate the superiority of the solution-processable $Ti_{0.95}Nb_{0.05}O_x$ charge carrier extraction layer, two references, Ca (4 nm)/Ag and LiF (1.5 nm)/Ag, deposited by thermal evaporation, were compared with our best interfacial condition. As shown in Fig. 4C, without sealing, the Ti(Nb)O_x-based PSC has the best stability: Its PCE only decreased by ~5% of its initial value after 1 week. The Ca/Ag-based PSC degraded the fastest, decreasing from its initial PCE by >30% after 1 day and by ~45% within 1 week. This difference is attributed to the fast oxidization of the very reactive Ca, leading to dramatic losses in J_{sc} and FF. The LiF/Ag-based PSC lost 15% of its initial PCE within 1 week. The extremely thin LiF layer (<2.5 nm, as required for efficient tunneling) (*46*) and the high sensitivity of LiF to moisture are likely to be responsible for the corresponding cell's inferior stability. It is possible that the stability of Ca- or LiF-based devices can be improved if they are thoroughly sealed. However, the requirement for sealing quality will be much more critical for Ca- and LiF-based devices than for the device based on the air-stable interface of $Ti_{0.95}Nb_{0.05}O_x$ (*39*).

The $Ti_{0.95}Nb_{0.05}O_x$ layer also shields the perovskite from the intrusion of humidity. It assumes a similar role in organic photovoltaic devices (*39*). We exposed bare $MAPbI_3$, $MAPbI_3$ with PCBM, and $MAPbI_3$ with PCBM and Ti(Nb)O_x to ambient air under room light for 3 weeks. A difference in color degradation associated with perovskite decomposition became clearly visible (fig. S14) (*14*). Thus, it appears that the hydrophobic nature of PCBM may protect the perovskite from reaction with water, and the coating of Ti(Nb)O_x could further enhance the stability.

Figure 4D also shows the long-term stability of PSCs that use the optimized inorganic charge extraction layers. The silver back contact was protected by a covering glass, which was separated from the front FTO glass by a UV-activated glue used as a sealant. The cells maintained 97% of their initial PCE after being kept in the dark for 1000 hours. Exposing the cells for 1000 hours in short-circuit conditions to full sunlight from a solar simulator resulted in a PCE degradation of less than 10%. This degradation was generally consistent across 10 devices (fig. S15) (*14*), indicating good long-term stability. During this time, an electric charge of around 72,000 C (4.49×10^{23} electrons) passed through the device. Thus, the planar cell structure and the metal oxide extraction layers, as well as the organometal halide perovskite material, are robust enough to sustain continued current flow under light exposure for 1000 hours. A further increase in the PCE without sacrificing stability could be obtained by varying the composition of the pervoskite, replacing, for example, part of the methylammonium cations in the $MAPbI_3$ pervovskite with formamidinium (*47*) and a small fraction of the iodide anions with bromide.

REFERENCES AND NOTES

1. G. Hodes, *Science* **342**, 317–318 (2013).
2. G. Xing *et al*., *Science* **342**, 344–347 (2013).
3. Q. Dong *et al*., *Science* **347**, 967–970 (2015).
4. M. Liu, M. B. Johnston, H. J. Snaith, *Nature* **501**, 395–398 (2013).
5. J. Burschka *et al*., *Nature* **499**, 316–319 (2013).
6. N. J. Jeon *et al*., *Nat. Mater.* **13**, 897–903 (2014).
7. N. J. Jeon *et al*., *Nature* **517**, 476–480 (2015).
8. W. S. Yang *et al*., *Science* **348**, 1234–1237 (2015).
9. J. H. Heo, H. J. Han, D. Kim, T. K. Ahn, S. H. Im, *Energy Environ. Sci.* **8**, 1602–1608 (2015).
10. W. Nie *et al*., *Science* **347**, 522–525 (2015).
11. J. H. Park *et al*., *Adv. Mater.* **27**, 4013–4019 (2015).
12. A. Mei *et al*., *Science* **345**, 295–298 (2014).
13. X. Li *et al*., *Energy Technol.* **3**, 551–555 (2015).
14. Materials and methods are available as supplementary materials on *Science* Online.
15. M. A. Green, K. Emery, Y. Hishikawa, W. Warta, E. D. Dunlop, *Prog. Photovolt. Res. Appl.* **23**, 1–9 (2015).
16. M. C. Beard, J. M. Luther, A. J. Nozik, *Nat. Nanotechnol.* **9**, 951–954 (2014).
17. E. Zimmermann *et al*., *Nat. Photonics* **8**, 669–672 (2014).
18. K. D. G. I. Jayawardena, L. J. Rozanski, C. A. Mills, S. R. P. Silva, *Nat. Photonics* **9**, 207–208 (2015).
19. Editorial, *Nat. Nanotechnol.* **9**, 657 (2014).
20. O. Malinkiewicz *et al*., *Adv. Energy Mater.* **4**, 1400345 (2014).
21. Z. Yang *et al*., *Nano Energy* **15**, 670–678 (2015).
22. M. Grätzel, *Nat. Mater.* **13**, 838–842 (2014).
23. M. Gunther, "Meteoritic rise of perovskite solar cells under scrutiny over efficiencies," *Chemistry World*, 2 March 2015; www.rsc.org/chemistryworld/2015/02/meteoritic-rise-perovskite-solar-cells-under-scrutiny-over-efficiencies.
24. H. Zhou *et al*., *Science* **345**, 542–546 (2014).
25. O. Malinkiewicz *et al*., *Nat. Photonics* **8**, 128–132 (2014).
26. Q. Lin, A. Armin, R. C. R. Nagiri, P. L. Burn, P. Meredith, *Nat. Photonics* **9**, 106–112 (2015).
27. A. G. Aberle, *Prog. Photovolt. Res. Appl.* **8**, 473–487 (2000).
28. M. A. Green, K. Emery, Y. Hishikawa, W. Warta, E. D. Dunlop, *Prog. Photovolt. Res. Appl.* **23**, 805–812 (2015).
29. M. A. Wittenauer, L. L. Van Zandt, *Philos. Mag. B* **46**, 659–667 (1982).
30. J. H. Kim *et al*., *Adv. Mater.* **27**, 695–701 (2015).
31. Z. Zhu *et al*., *Angew. Chem. Int. Ed.* **53**, 12571–12575 (2014).
32. C. Wu, C. Yang, *Sol. Energy Mater. Sol. Cells* **132**, 492–498 (2015).
33. Y. H. Kim *et al*., *Adv. Funct. Mater.* **21**, 1076–1081 (2011).
34. W. Chen *et al*., *Energy Environ. Sci.* **8**, 629–640 (2015).
35. N. Alidoust, M. C. Toroker, J. A. Keith, E. A. Carter, *ChemSusChem* **7**, 195–201 (2014).
36. U. S. Joshi, Y. Matsumoto, K. Itaka, M. Sumiya, H. Koinuma, *Appl. Surf. Sci.* **252**, 2524–2528 (2006).
37. Z. Huang *et al*., *RSC Adv.* **4**, 60670–60674 (2014).
38. J. Deng, M. Mortazavi, N. V. Medhekar, J. Zhe Liu, *J. Appl. Phys.* **112**, 123703 (2012).
39. K. Lee *et al*., *Adv. Mater.* **19**, 2445–2449 (2007).
40. T. Kuwabara, T. Nakayama, K. Uozumi, T. Yamaguchi, K. Takahashi, *Sol. Energy Mater. Sol. Cells* **92**, 1476–1482 (2008).
41. T. Kuwabara, H. Sugiyama, T. Yamaguchi, K. Takahashi, *Thin Solid Films* **517**, 3766–3769 (2009).
42. K. Wojciechowski, M. Saliba, T. Leijtens, A. Abate, H. J. Snaith, *Energy Environ. Sci.* **7**, 1142–1147 (2014).
43. Y. Furubayashi *et al*., *Appl. Phys. Lett.* **86**, 252101–252103 (2005).
44. S. Braun, W. R. Salaneck, M. Fahlman, *Adv. Mater.* **21**, 1450–1472 (2009).
45. J. H. Heo *et al*., *Adv. Mater.* **27**, 3424–3430 (2015).
46. X. Liu *et al*., *ACS Appl. Mater. Interfaces* **7**, 6230–6237 (2015).
47. J. Liu *et al*., *Adv. Mater.* **27**, 4918–4923 (2015).

ACKNOWLEDGMENTS

This work was partially supported by the Core Research for Evolutional Science and Technology of the Japan Science and Technology Agency. The authors thank H. Kanai at the Materials Analysis Station of the National Institute for Materials Science, Japan, for high-resolution SEM image measurement and T. Shimizu and T. Ishikawa for technical support. L.H. thanks for H. Naito of Osaka Prefecture University and M. Shimizu of the Institute of Advanced Energy, Kyoto University for their useful discussions. M.G. acknowledges financial support of this work under the Swiss Nanotera and Swiss National Science Foundation PV2050 program and acknowledges his affiliation as a visiting faculty member with Nanyang Technological University, Singapore and the Advanced Institute for Nanotechnology at Sungkyunkwan University, Suwon, South Korea.

SUPPLEMENTARY MATERIALS

www.sciencemag.org/content/350/6263/944/suppl/DC1
Materials and Methods
Figs. S1 to S15
Tables S1 to S3
References (*48–50*)

27 July 2015; accepted 14 October 2015
Published online 29 October 2015
10.1126/science.aad1015